Additive manufacturing of high-performance, flexible 3D siloxane-based scintillators through the sol-gel route

Sara Maria Carturan [a,b,*], Hanna Skliarova [b], Giorgia Franchin [b,c,*], Giada Bombardelli [c], Alice Zanini [c], Felix Eduardo Pino Andrades [a], Jessica Carolina Delgado Alvarez [a], Sandra Moretto [a,d], Gianluigi Maggioni [a,b], Walter Raniero [b], Devid Maniglio [e,f], Anna Paola Caricato [g,h], Alberto Quaranta [e,f]

[a] *Department of Physics and Astronomy "Galilei", University of Padova, Via Marzolo 8, 35121, Padova, Italy*
[b] *INFN Laboratori Nazionali di Legnaro, Viale dell'Università, 2, 35020, Legnaro (PD), Italy*
[c] *Department of Industrial Engineering, University of Padova, Via Marzolo 9, 35121, Padova, Italy*
[d] *INFN Sezione di Padova, Via Marzolo 8, 35121, Padova, Italy*
[e] *INFN TIFPA, Trento Institute for Fundamental Physics and Applications, Via Sommarive 14, 38123, Povo, Trento, Italy*
[f] *Department of Industrial Engineering, University of Trento, Via Sommarive 9, 38123, Povo, Trento, Italy*
[g] *Department of Mathematics and Physics "Ennio de Giorgi" University of Salento, Via per Arnesano, 73100, Lecce, Italy*
[h] *INFN Sezione di Lecce, Via Provinciale per Arnesano, 73100, Lecce, Italy*

ARTICLE INFO

ABSTRACT

A novel method for the production of high-performing, flexible 3D-printed siloxane-based scintillators is here described. It consists in the synthesis *via* sol-gel of phenyl-bearing siloxane resins with methacrylate functionalities suitable of photopolymerization by UV illumination, therefore shaped at desired geometries through additive manufacturing, namely digital light processing (DLP). Both hydrolytic and non-hydrolytic sol-gel approaches are adopted to promote the reactivity of diphenyl bearing alkoxysilane precursors and to control phase separation of dimethyl and diphenyl rich domains. The structural evolution during the sol-gel reactions is investigated by Fourier transform infrared spectroscopy (FTIR), which is also exploited to assess photocuring, after addition of diphenyl 2,4,6 trimethyl - benzoyl phosphine oxide (TPO) as UV initiator. The optical properties after addition of suitable fluorophores are studied by excitation/emission spectroscopy. Once defined the best formulations as for optical clarity, mechanical toughness and extent of photocuring, thin disks of scintillators are produced by UV illumination and exposed to α particles to define the light output values. The gathered scintillation light has been compared to the one from standard, non-flexible plastic scintillator EJ-212, resulting in values up to 44%. Photorheology is used to assess the printability by DLP, monitoring UV curing times and complex modulus plateau. Tensile tests are performed aiming to observe the stress-deformation behaviour of representative siloxane-based resins obtained by either simple casting or DLP, to get insight on possible variations induced by the fabrication technology. To assess printing resolution and capabilities, selected formulations of photocurable polysiloxanes scintillators are 3D printed by DLP in forms of benchmark shapes, i.e. gyroid and Kelvin cell, and printing quality is derived by scanning electron microscopy (SEM), while their scintillation upon 4.5 MeV H^+ ion beam irradiation is gathered by CCD camera observations, affording beam spot image reconstruction.

1. Introduction

Organic scintillators have been extensively used since the late '70 s to reveal ionizing particles, γ-rays, β-rays and fast neutrons in a huge number of applications related to nuclear physics and high energy physics experiments, dose monitors in power plants and nuclear medicine sites, homeland security at borders. Their main advantages are lightweight, low cost, fast response, ease of manufacturing and high hydrogen content for fast neutrons detection. As compared to inorganic scintillators, they suffer from low light yield, low average atomic number, lowering the interaction with low Linear Energy Transfer (LET) radiation, nonlinear response with particle energy, and limited radiation

---

hardness. However, organic scintillators are beneficial for high detection volume: a variety of complex shapes and geometries are currently in use to maximize interaction with impinging radiation, to improve scintillation light harvest and delivery to photosensors, and to enhance granularity of light signal collection. Further development is ongoing to enhance imaging resolution and responsivity of the whole detector [1–3],. In nuclear medicine, organic scintillators offer the unique advantage of fast response and water equivalence, extending the use as radiation dosimeters both in liquid and solid form [4]. In the case of proton therapy (PT), whose application in specific treatment plans is hugely spreading, the use of plastic scintillators allows precise beam profile reconstruction, in relation to both energy loss vs penetration depth, i.e. Bragg curve, and high-resolution 3D imaging [5–8],. Localized tumours treatment with proton beams may outperform radiotherapy, though limitations in cancer treatment plans still exist, mainly arising from the specific physics underlying the use of proton beams; since linear energy transfer (LET) of high energy protons displays maximum energy deposition at the end of the particle range, a strict and precise control of the delivered dose is required in order to assure that negligible energy is released to healthy tissues.

For this reason, a growing effort from the radiation detectors research community is soaring and a significant number of 3D scintillator detectors, including miniaturized, flexible and in vivo detectors, is at hand to provide the greatest accuracy in dose-depth determination during PT treatment and to monitor undesired dose to healthy organs [7, 9,10]. Whitin this state of art, the possibility to design curved shapes, awkward geometries and carved structures as a mimic of the human body can lead to enhanced compliance of the model to the real situation, providing better accuracy in dose delivery and treatment efficacy.

In the last decade, additive manufacturing of plastic scintillators has been pursued, focusing on the traditional rigid polymer matrices, used to produce standard scintillators, i.e. polystyrene or polyvinyltoluene, such as BC400 (Saint Gobain) and EJ-200 (Eljen Technology). Plastic scintillators based on vinyl polymer have been obtained by Fused Filament Fabrication (FFF) [11] and proved to reach good values in terms of light yield, although the relatively high temperature (~250 °C) of the printing process might lead to unpredictable variation in additives distribution [12]. Higher printing resolution and room temperature fabrication is achieved by Digital Light Processing (DLP). This approach requires a base resin with UV curing capability, where the initiator, typically a phosphine oxide, undergoes bonds rupture leading to free radicals resulting in a fast polymerization process. Vinyl-based polymers are not appropriate materials, owing to the impervious UV photocuring of the base monomer [13]. To overcome this drawback, bisphenol acrylates with suitable dispersible fluorophores have been prepared for the fabrication of scintillators [13,14]. High phenyl concentration is crucial to achieve intrinsic fluorescence emission, also enhancing the solubility of primary dye and wavelength shifter into the base resin [15]. By exploiting bisphenol acrylate derivatives, plastic scintillators produced by DLP with optimal pulse shape discrimination capability have been produced by over doping the base formulation with suitable primary dye, while preserving printability and printing resolution [16]. Currently, 3D printing of tumour models made of plastic scintillators by additive manufacturing has been pursued and proved to be useful as volumetric dosimeters to evaluate the tumour absorbed dose [17,18]. Organic scintillators based on polysiloxane are known to display optimal performance as related to light output, response time and radiation resistance [19]. Recently, siloxane resins prepared from commercial sources and added with fluorene-based fluorophores displayed optimal light yield values and n/γ discrimination capability with performance holding constant or even improved at operating temperatures up to 50 °C [20,21]. Moreover, these materials typically possess elastomeric behaviour, i.e. they are soft, pliable, foldable and compressible.

Accordingly, silicones are the material of choice to meet the growing need in radiotherapy of mouldable materials to produce customized boluses or deformable phantoms [22]. Furthermore, in proton therapy

plans, where the target organ undergoes undesired, but unavoidable, shifts during irradiation, the possibility to achieve time-resolved imaging may largely improve the accuracy of dose distribution [23].

However, silicone-based systems with light yield comparable to traditional plastics are limited to formulations based on commercial resins [21], which reduce their versatility and tailoring to specific needs and applications.

The goal of this work is to synthesize a polysiloxane resin with the following distinctive features:

- UV photocuring by suitable addition of photoinitiator and exposure to moderate power UV lamp (20–50 mW/cm^2) in the near UV range (360–400 nm);
- high concentration of phenyl moieties to spring intrinsic fluorescence, and in turn scintillation upon irradiation;
- dissolution ability of the fluorophores to design a scintillator material (i.e. primary dye and wavelength shifter);
- good scintillation yield as exposed to standard radioactive sources;
- printability at acceptable times and resolution, assessed by fabrication of selected benchmarking shapes *via* DLP.

The sol-gel route has been chosen to pursue these aims, owing to the versatility of the technique, which affords macromolecules composed of strong Si-O-Si bonds, and "decorated" with lateral or terminal substituents with potentially any desired organic functionality, tailored by the selection of alkoxysilane precursors. This way it is possible to introduce phenyl groups, to generate intrinsic fluorescence, or alkyl groups with different chain length to modify flexibility or hydrophobicity, or to enhance the solubility of added fluorophores, or even acrylate groups to enable UV photocuring. Previous literature, relevant to photocurable siloxanes *via* sol-gel process, has been reviewed and provided useful hints to fulfil the mentioned requirements [24–26]. The preparation of this class of silica-based hybrids might be tricky for specific cases where total removal of water or solvent is mandatory to achieve fully homogeneous, compact and transparent materials. For this reason, besides the classical hydrolytic sol-gel synthesis, non-hydrolytic route has been pursued [27–29].

Even though prior art on the sol-gel synthesis of polysiloxanes has been reported, the experiments reported herein depart from the designed formulations in literature in that phenyl, - dimethyl, -methacrylate substituents have been used in the same batch in order to provide UV-curing ability, deformability and intrinsic fluorescence of the prepared resins. Previous literature studies on the comparison between hydrolytic and non-hydrolytic routes focused on the use of diphenyl and methacrylate bearing silane precursor, and in-depth investigation on the mechanism leading to the production of oligomers has been postulated and supported by analyses [29,30]. In the hydrolytic route, a more complete condensation degree was demonstrated, but this approach has the drawback of leaving traces of solvent and water, as highlighted in ref. [31]. As a result, since the formulations herein produced and described above make use of different silane precursors and the final outcome in function of different synthetic route has not been reported in literature, we explored both pathways, using infrared spectroscopy to derive structural evolution.

2. Materials and methods

2.1. Materials

Di-functional diphenylsilanediol (DPSi(OH)$_2$) 98% purity from Alfa Aesar, diphenyl dimethoxysilane (DP-DMOS) >98% purity from TCI, dimethyl diethoxysilane (DM-DES) 97% purity from Sigma-Aldrich, tri-functional methacryloxypropyl trimethoxysilane (MA-TMOS) 98% purity from Sigma Aldrich and methyltriethoxysilane (MTES) 95% purity from Acros were used as received. 2-methyl tetrahydrofuran >98% purity from TCI was used as solvent. Ba(OH)$_2$·H$_2$O (95% purity, Alfa

Aesar) was used as catalyst for base-catalyzed sol-gel, while hydrochloric acid 1 M, prepared from HCl 37% (Carlo Erba) was used for acid-catalyzed sol-gel.

Diphenyl(2,4,6-trimethylbenzoyl)phosphine oxide (TPO) >98% purity from TCI was used as a photoinitiator for UV-curing. As for fluorophores, 2,5-diphenyloxazole (PPO) 99% purity from Acros Organics was used as primary dye; Lumogen Violet (LV) perylene diimide dye >98% purity from BASF was chosen as wavelength shifter.

2.2. Synthesis of polysiloxane oligomers

Polysiloxanes were obtained by catalytic (acidic or basic) hydrolytic or non-hydrolytic sol-gel synthesis. For the acid-catalyzed sol-gel, a mixture of alkoxysilane precursors, bearing di- or tri- hydrolyzable -OR groups were chosen to afford the required functionalities, i.e. acryl- and phenyl- groups. Besides selected precursors, we added dimethyl diethoxysilane or methyltriethoxysilane to vary the mechanical stiffness of the polymer. The same approach was followed in the case of non-hydrolytic synthesis, where diphenylsilanediol reacted with dimethyl diethoxysilane as a "spacer" to reduce chain rigidity, induced by the encumbrance of phenyl groups that hinders the rotational freedom of Si-O-Si bonds. The formulations used for the synthesis are summarized in Table 1, where distinctive features as for molar ratios between relevant functional groups are also reported.

2.2.1. Hydrolytic sol-gel process

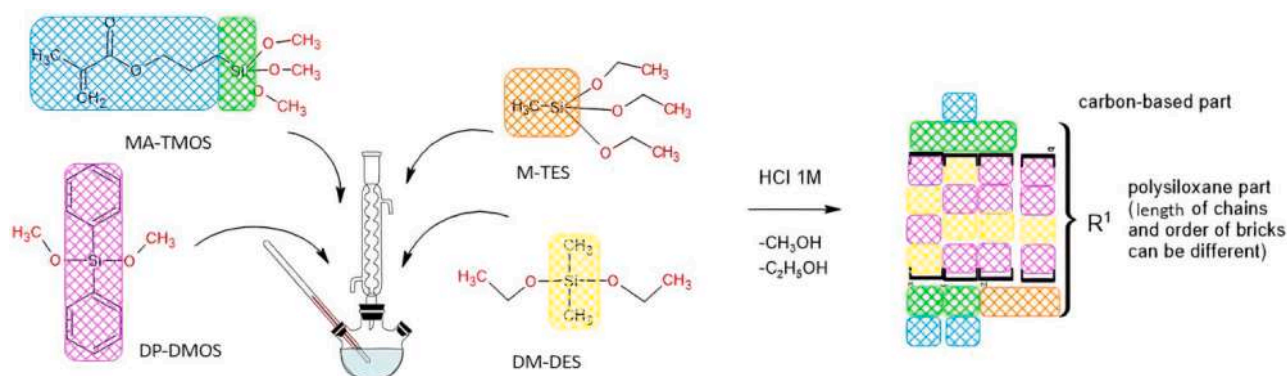The resins with H- ending label in Table 1 were synthesized via an acid-catalyzed hydrolytic sol–gel reaction with different molar ratios of diphenyl dimethoxy silane (DP-DMOS), methacryloxypropyl trimethoxysilane (MA-TMOS), dimethyldiethoxysilane (DM-DES) and methyltriethoxysilane (M-TES), as reported in Table 1 and schematized in Fig. 1. After dissolution of the precursors in the solvent (2-methyl THF) in a three-necks flask (50 mL capacity) equipped with a reflux condenser, a diluted HCl aqueous solution (1 M, 0.5 M or 0.1 M) was added to the mixture, at the molar ratio water/-OR groups 1/1, and stirred for 20 min. The reaction mixture was kept under stirring at 60ºC overnight. Just as an indication of the reaction volume, the amount of used solvent was in the range 10–15 mL.

The solvent and the by-products, methanol, ethanol and residual water, were evaporated in vacuum leading to a viscous transparent resin with a faint yellow colour, whose intensity faded as HCl concentration was lowered.

2.2.2. Non-hydrolytic condensation

The -NH resins were prepared dissolving the precursors, see Table 1, in 2-methyl THF (20% wt), in the presence of Ba(OH)$_2$ as catalyst (0.10–0.15 mol% to the total monomers) to promote the condensation between precursors.

As a general route, MA-TMOS and Ba(OH)$_2$ were mixed with a small amount of 2-methyl THF in a three-necks flask equipped with a reflux condenser and a thermometer. As an indication of the total volume of the reaction mixture, the experiments were conducted using about 10–15 mL of solvent, in a 50 mL capacity, three necks flask. The mixture was heated up to 60 ºC, then diphenylsilanediol was added in small

Table 1

Preparation details of UV curable polysiloxanes produced by hydrolytic (H-ending) and non-hydrolytic (NH- ending) sol-gel.

Label	Composition	mol% Si precursor	Mol -OH/mol -OR	Mol acryl/ total	Di/tri functional	Mol phenyl/mol Si	Catalyst
DPDMM_H—H	MA-TMOS	10	–	0.10	4.3	0.40	HCl 1M
	DP-DMOS	20					
	DM-DES	61					
	M-TES	9					
DPDMM_L-H	MA-TMOS	10	–	0.10	4.3	0.40	HCl 0.1M
	DP-DMOS	20					
	DM-DES	61					
	M-TES	9					
DPDMM_M-H	MA-TMOS	10	–	0.10	4.3	0.40	HCl 0.5M
	DP-DMOS	20					
	DM-DES	61					
	M-TES	9					
DPDM50-NH	MA-TMOS	20	0.83	0.20	4.0	1.00	Ba(OH)2
	DPSi(OH)2	50					
	DM-DES	30					
DPDM60-NH	MA-TMOS	25	1	0.25	3.0	1.12	Ba(OH)2
	DPSi(OH)2	56					
	DM-DES	19					
DP50-NH	MA-TMOS	50	0.67	0.50	1.0	1.00	Ba(OH)2
	DPSi(OH)2	50					

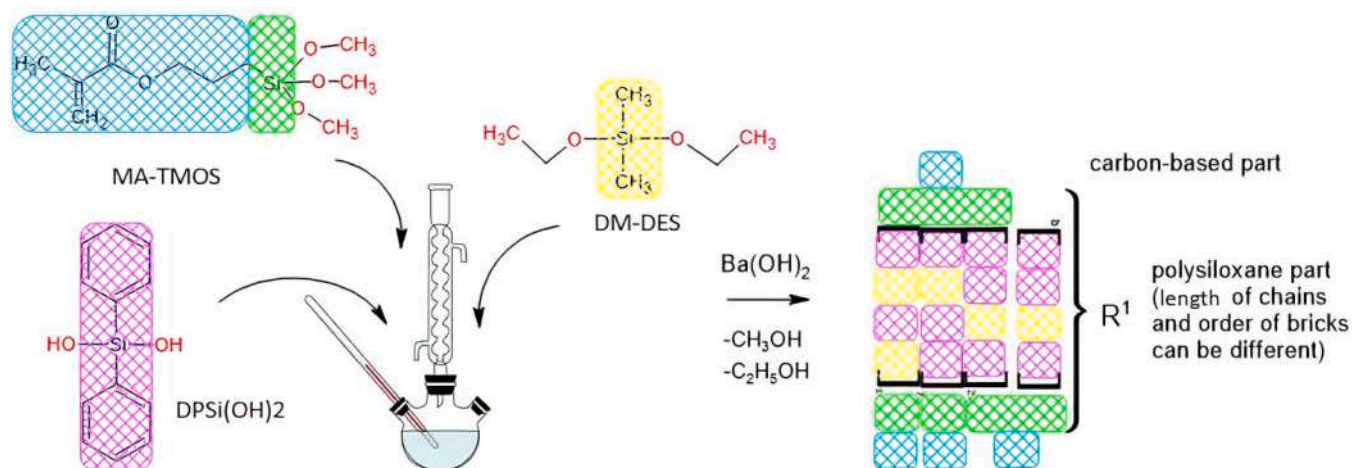**Fig. 1.** Schematic view of acid catalyzed sol-gel pathway.

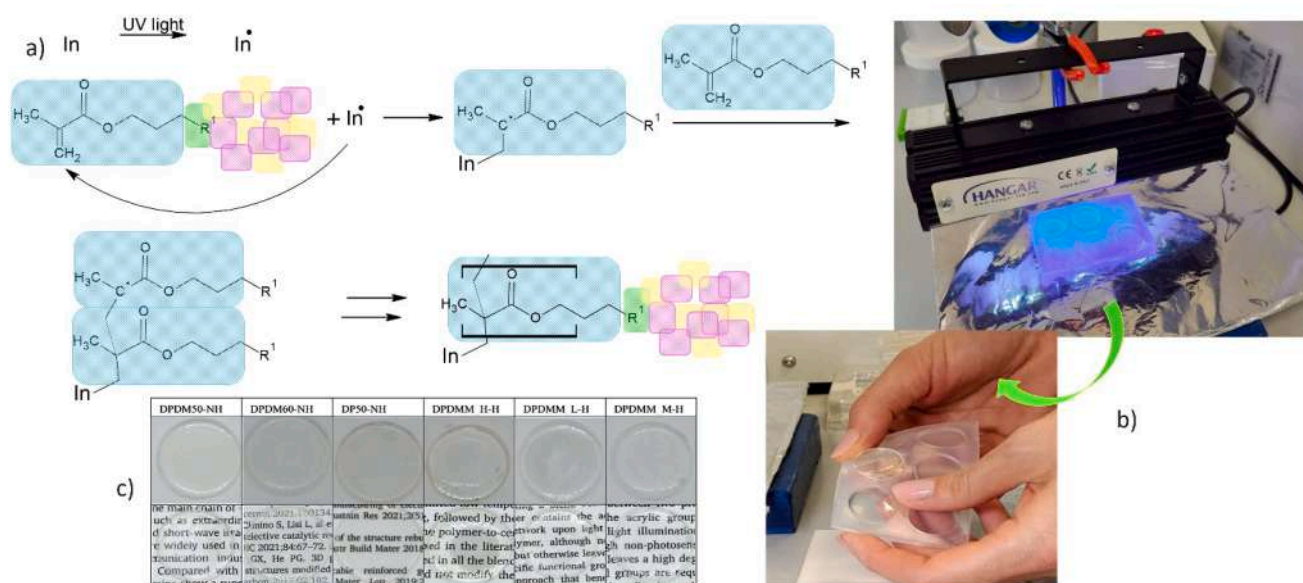**Fig. 2.** Schematic view of base-catalyzed non-hydrolytic sol-gel pathway.

Fig. 3. a) Sketch of chemical reactions involved in UV photocuring process; b) liquid doped polysiloxane resins under UV-irradiation and samples extraction from the mold; c) photos of the obtained disks of polysiloxane scintillators after UV photocuring.

portions during about 2 h. The reaction mixture was kept stirred at 75–80 °C overnight. The process is schematized in Fig. 2.

After cooling, volatile by-products, i.e. methanol and ethanol, were removed in vacuum, leaving residue of 2-methyl THF. The resins were filtered from white solid particles, composed of insoluble catalyst and unreacted precursor, using 0.40 μm Teflon filters providing transparent colourless viscous liquids.

2.3. Photocurable formulations and UV curing

The liquid resins were transferred in amber glass vials and added with photoinitiator (TPO, 1% wt.), primary dye (PPO, 1% wt.) and wavelength shifter (LV, 0.02% wt.); the mixtures were kept under stirring overnight at 60 °C, leading to complete dissolution of the additives.

About 0.35 g of each mixture was poured into a transparent silicone mold and exposed to the benchtop UV lamp (Hangar, λ_{max} 365 nm, power 20 mW/cm^2 [1]) for 15 min. Thin solid disks with thickness ranging from 0.45 to 0.74 mm and diameter 20 mm were extracted from the mold and further heated for 2 h in static oven at 50 °C up to complete removal of volatiles. The UV curing process scheme and photos of the produced samples have been reported in Fig. 3.

2.4. Analytical techniques

Chemical evolution during the sol-gel synthesis and subsequent UV-induced polymerization process were studied by FTIR spectroscopy in the range 4000–400 cm^{-1}, resolution 4 cm^{-1}, using a Jasco FT/IR-400/600 plus model, equipped with attenuated total reflectance (ATR), using single reflection diamond crystal as dispersing element.

Photophysical properties of both the liquid resins and the UV cured samples in form of disks have been studied by excitation/fluorescence spectroscopy in front-face geometry, using a Jasco FP-6300 spectrofluorimeter, equipped with a 150 W Xe lamp; the spectra were collected at room temperature.

Photorheological tests were conducted on the fluid doped resins using a rotational rheometer (Kinexus Lab+; Netzsch, Germany) equipped with a UV-plate system accessory (KNX5007, Netzsch, Germany) with a 40 mW/cm^2 UV lamp filtered at 365 nm. The analysis

---

[1] Irradiance power was evaluated at a fixed distance from the mold (around 10 cm) using a Luxmeter (Delta-OHM HD2302)

employed a 8 mm parallel plate geometry with a gap of 0.5 mm. Storage (G') and loss shear moduli (G") were measured as a function of time at a constant frequency of 1 Hz. The UV light was switched on after a period of 60 s and kept on throughout the measurement, during which the system was allowed to stabilize; a baseline was recorded, and, with the advancement of the photocuring process, changes in the moduli were monitored and correlated with the gel point, the structural densification, the mechanical properties and the degree of cross-linking.

As for the printing quality of the objects produced by DLP, it was analyzed by Scanning Electron Microscopy (SEM, Tescan, model VEGA 3 XM).

Mechanical tensile tests were performed using a universal testing machine (Quasar 25, Galdabini s.r.l., Italy), equipped with a load cell of 10 N and operating with a crosshead speed of 10 mm/min, on DPDM60-NH and DMDM50-NH to test elongation and to evidence tensile strength variation of samples achieved using the same resin either cast or DLP printed. To this aim, dogbone specimens have been produced according to ISO 527–2 2012 regulations (Appendix A, sample type 1BB[2]). 5 to 10 specimens were tested for each composition and fabrication route; results are reported in terms of mean values ± standard deviation. Printing plane of DLP samples was perpendicular to the tensile strain direction.

2.5. Light yield measurements

In order to estimate the scintillation yield and decay time of the polysiloxane disks described above, the samples were optically coupled to a 1″ diameter photomultiplier tube (PMT, Hamamatsu H6524, operated at −1500 V) and an ^{241}Am calibration α source (Eα ~5.5 MeV, activity ~30 kBq, active spot diameter 5 mm) was set on the opposite face of the sample, with an air gap of 4 mm between the source and the sample. The arranged set-up was enclosed in a light-tight black box, to enhance scintillation light collection by the photosensor and minimize noise from ambient light. The PMT signals were acquired and preprocessed using a CAEN digitizer V1730 (14-bit ADC resolution and 500 MHz of the sampling rate), which is running the firmware DPP-PSD (digital pulse processing for charge integration). To determine the decay time of the scintillation signals, a set of waveforms was digitized using a Teledyne LeCroy oscilloscope HDO4104 model, having 12-bit ADC resolution, 1 GHz bandwidth and sampling up to 2.5 GS/s. The PMT bias voltage was applied using a CAEN V6533 VME HV Power Supply Module, controlled by a CAEN V2718 VME to USB 2.0 unit. A CAEN A4818 USB 3.0 to CONET2 Adapter was used to communicate (configuration and data acquisition) between a desktop PC and the digitizer. All parameters for data acquisition were managed using ABCD (Acquisition and Broadcast of Collected Data) software [32] as an opensource project. To perform a light output comparison of the photocured polysiloxane samples, the same measurement was carried out using an EJ-212 standard plastic scintillator (diameter 25 mm, thickness 0.5 mm, from Eljen Technology Texas-USA).

2.6. DLP printing of selected scintillator formulations

3D printing of the polysiloxane scintillators was pursued using a DLP printer (Pico 2, Asiga, Japan), with a working wavelength of 385 nm, a light intensity of 30 mW/cm^2 and a projector pixel size of 62 μm. The fluid resins to be printed by DLP were selected on the basis of photo-rheological tests; prior to printing, their curing depth was determined with a micrometer screw gauge by measuring the thickness of the cured portion of ink droplets (50 μL) illuminated with the projector for 30 s and then soaked in isopropanol. Layer height and exposure time were varied to optimize printability in terms of resolution, printing speed and curing degree of the resin. Specific shapes from computer-aided design,

i.e. gyroid and Kelvin cell, were fed to the printer software, aiming at the assessment of accuracy in 3D reproduction of complex geometries with carved structures and regularly spaced cavities. All models had nominal dimensions of 11.5 x 11.5 x 11.5 mm^3 and a strut size (Kelvin cell) or wall thickness (gyroids) of 400 μm. In some cases, the final 3D printed object was further exposed to UV for post-curing using a tabletop UV-furnace.

2.7. Proton beam irradiation of disks and 3D printed shapes

Some formulations in the form of thin disks (thickness 0.45 – 0.74 mm) and 3D printed shapes were exposed to a proton beam (4.5 MeV), collimated to achieve different spot sizes. The beam current was kept in the range 16–18 nA, thus the proton fluence was in the range 5×10^{10} - 3 $\times 10^{11}$ H^+/cm^2 s, depending on current and beam size. The spot dimensions (diameter 6 mm and 17 mm) were varied to irradiate either a central portion of the sample and the entire surface, meanwhile providing a variation in the proton flux. Once the samples were inside the irradiation chamber, as described in section 3.6, they were exposed to the beam: the scintillation light was gathered using a CCD camera (ATIK 420 colour, with an appropriate objective to focus on the position of the sample), located outside the vacuum chamber and coupled to a lateral viewport so that the irradiation spot lied in the CCD camera line of sight. Consecutive images were recorded by setting the exposure time in the range 0.05 s ÷ 1 s.

3. Results and discussion

3.1. Infrared characterization

3.1.1. Hydrolytic sol-gel process

Infrared spectra of precursors are reported in Fig. 4a, as well as of DPDMM_H—H obtained after one night at 60 °C and solvent removal. In the case of MA-TMOS signals are visible at 2845 cm^{-1} (C—H stretching in methoxy group), 1717 cm^{-1} (C = O stretching), 1638 cm^{-1} (C = C symmetric stretching), 1322 and 1295 cm^{-1} (C—O-C asymmetric and symmetric stretching, respectively), 1160 cm^{-1} (-CH$_3$ deformation), 1078 cm^{-1} (Si-O-C asymmetric stretching), 940 and 815 cm^{-1} (C = C and C = O deformation asymmetric and symmetric, respectively) [33], though at 940 cm^{-1} the signal from Si-O-C stretching absorption might be overlapping.

As regarding M-TES, the signal at 2974 cm^{-1} is ascribed to asymmetric stretching of -C-H in the Si-CH$_3$ group and is associated with the peak at 1390 cm^{-1} (-C-H bending mode), while the absorption at 1275 cm^{-1} is attributed to Si-C bond stretching [34]. For the precursor DP-DMOS, relevant signals are related to the presence of phenyl substituents: in the range 3060–3040 cm^{-1} C-H stretching in phenyl ring, at 1590 cm^{-1} C-C ring vibration, at 1430 cm^{-1} Si-C stretching of Si-phenyl, while in the low frequencies region (750–500 cm^{-1}) several modes related to ring deformation are observed [35]. As for DM-DES, typical signals and assignments are very similar to those of M-TES described above.

After hydrolysis and condensation reactions proceeded overnight (Fig. 1), the chemical structure of the network undergoes remarkable changes, as highlighted by variation of main IR signals, thus pointing to an optimal extent of the process. The spectrum of the resin displays the relevant features ascribed to diphenyl and dimethyl moieties, Si-OR signals being negligible. The intense broad band at 1050–1010 cm^{-1} suggests the occurrence of Si-O-Si bridging bonds indicating that siloxane-based network is formed [36]. The effect of varying the concentration of HCl has been also investigated: the spectra of the different formulations are reported in Figure S1. No significant changes appear as related to the main features of the hydrolysis and condensation products.

The extent of UV-induced polymerization may be evaluated by observing the behaviour of acryl groups: once the sol-gel process has led to the siloxane network after one night of reaction, the C = O bond
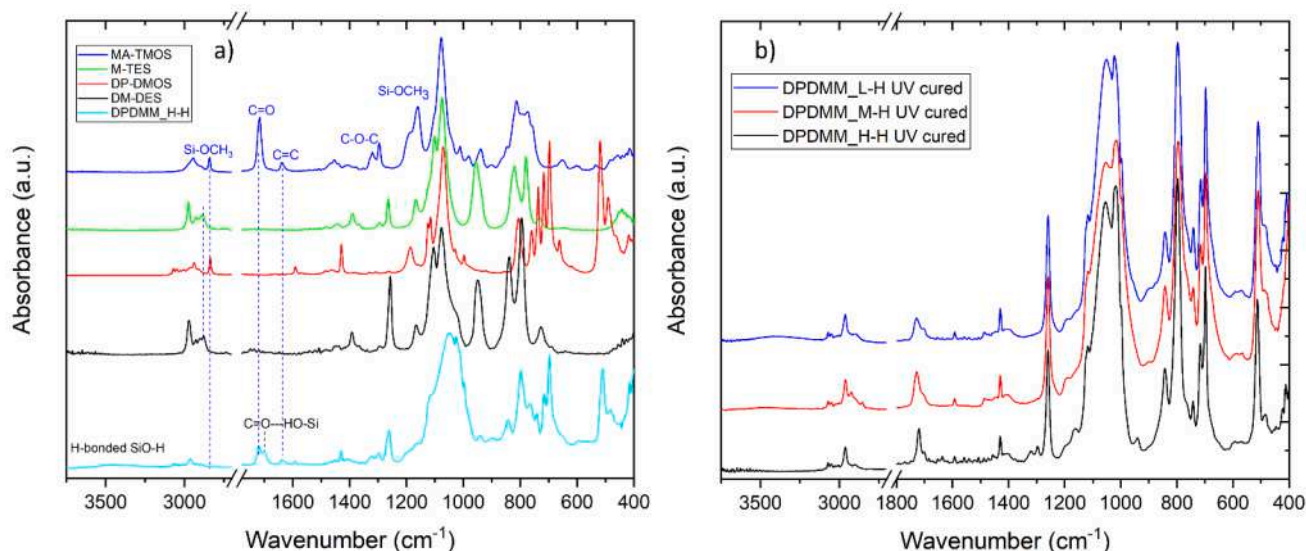

Fig. 4. Infrared spectra of a) sol-gel precursors and reaction product in case of hydrolytic route using 1 M HCl as catalyst and b) resins obtained with different HCl concentrations after UV curing. (For interpretation of the references to colour in this figure legend, the reader is referred to the web version of this article.)
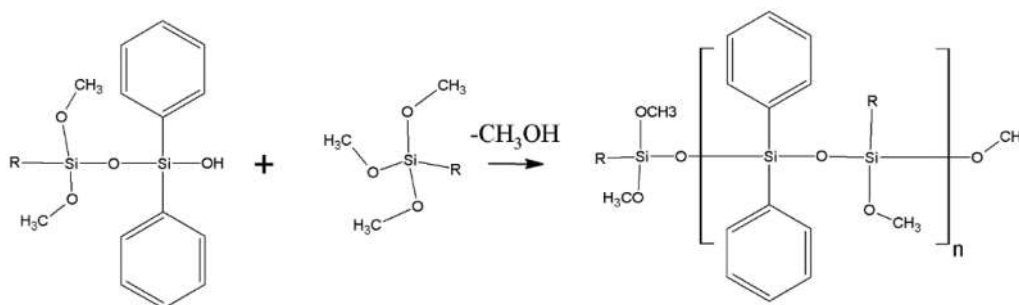

Fig. 5. Alkoxylation reaction between MA-TMOS and DPSi(OH)$_2$.

stretching absorption is split in two close components at 1718 and 1700 cm^{-1} [37]. This is ascribed to conjugation of carbonyl group to residual Si-OH, i.e. hydrogen bonded species -C = O—HO-Si≡, that causes a shift at lower frequency of the C = O stretching absorption. Indeed, after UV curing negligible -Si-OH groups remain with complete disappearance of the broad band at 3450 cm^{-1} and drop of the signal at 1700 cm^{-1} (Fig. 4b). This holds true for the resin prepared using HCl 1 M and 0.5 M, whereas in the case of 0.1 M weak signals indicating a lower condensation degree are visible at 3450 and 1700 cm^{-1}, related to the presence of residual Si-OH. For all the formulations, after UV exposure the C = C

signal at 1636 cm^{-1} almost disappears, indicating optimal extent of the photocuring process (Fig. 3).

3.1.2. *Non hydrolytic sol-gel process*

According to literature [38], the success of hybrid polysiloxane formation relies on the alkoxylation mechanism, as described below in Fig. 5.

The MA-TMOS:DPSi(OH)$_2$ 2:3 molar ratio should provide diphenylsiloxane units alternated by three-way cross-linking sites from MA-TMOS (Fig. 6).
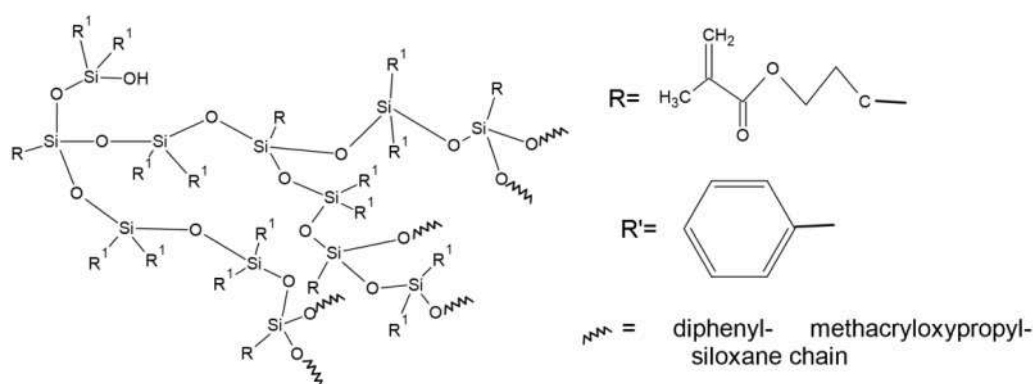

Fig. 6. Expected siloxane network in case of stoichiometric molar ratio between MA-TMOS and DPSi(OH)$_2$.
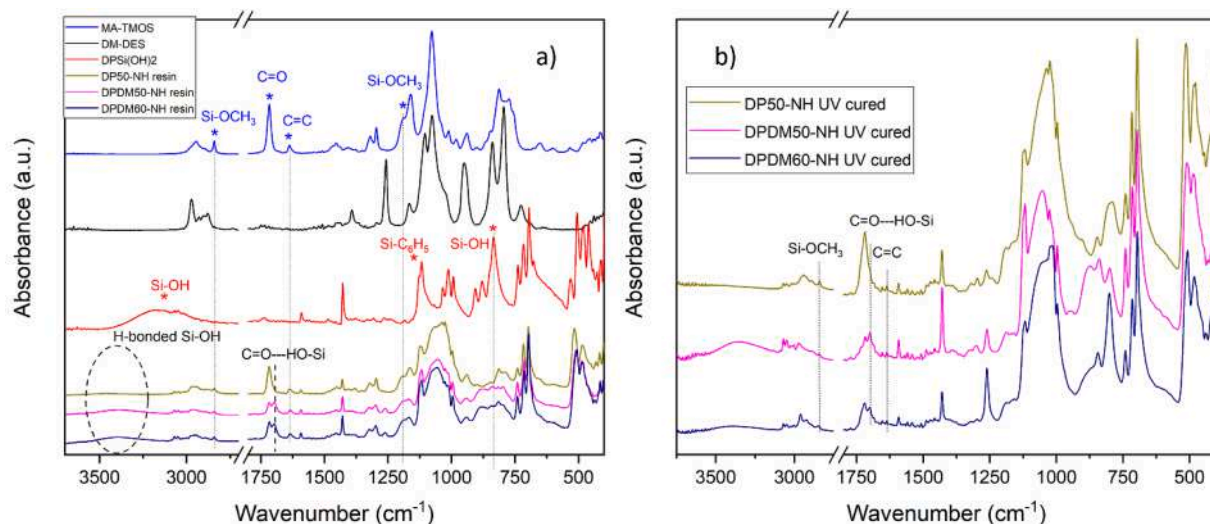
Fig. 7. FTIR spectra of precursors and products of the non-hydrolytic production process in case of methacrylate-siloxane before (a) and after (b) UV induced photo crosslinking.

This process has been extensively studied and the products have been characterized in terms of molecular structure, even in function of different molar ratios between reactants [29,39,40]. Several analytical techniques point to a final structure mostly linear or composed of cyclic oligomers with few branching sites. The sterical hindrance of both methacrylate and diphenyl groups accounts for a limited extent of alkoxylation, besides the specific solid-liquid interaction of the insoluble $Ba(OH)_2$ catalyst. Furthermore, as the molar percentage of $DPSi(OH)_2$ exceeds 50%, chain extension is even more hampered and the structure is mainly composed of branched, short chains, preluding to a rigid material after UV curing. In the present work, $DPSi(OH)_2$ has been used for alkoxylation not only with MA-TMOS but also with DM-DES and the structural evolution during the process has been evaluated by infrared spectroscopy (Fig. 7a).

In all cases, the final product is a polysiloxane, as proved by the appearance of the intense, wide band at 1100–1000 cm^{-1}. Irrespectively of the absence of added water, the DPDM50-NH and DPDM60-NH products display splitting of C = O signal at 1728 and 1700 cm^{-1} due to conjugation with -OH groups, pointing to the presence of unreacted $DPSi(OH)_2$. In literature, this behaviour is related to diphenylsilanediol exceeding 50% mol, while in the present case the unreacted silanol is clearly visible in both 56% mol (DPDM60-NH) and 50% mol (DPDM50-NH). Hence, a detrimental effect on alkoxylation progress due to the presence of dimethyldiethoxysilane is envisaged. In the case of DP50-NH, where dimethyl units are absent, the silanol induced signals are less intense, thus confirming previous literature data. To support the reliability of our data, DP60-NH has been synthesized and the comparison between infrared spectra is reported in Figure S2 (SI). As $DPSi(OH)_2$ exceeds 50% mol the splitting of C = O and the broad band due to -OH stretching leap out.

As for the extent of photocuring, it is worth to note that the formulations containing dimethyl units display a remarkably high completion of the process, comparable to the DP derived one as evidenced in Fig. 7b by the negligible presence of the vinyl peak at 1635 cm^{-1}. This is expected, taking into account the much higher concentration of acrylic functionalities in the case of DP only formulations, as highlighted in Table 1.

As for the comparison between the two processes, the spectra of the UV cross-linked polysiloxanes with the same starting composition (Figure S3) deserve some comments. In both cases, evident clues of incomplete condensation are observed, though in case of hydrolytic pathway hydrolysis of methoxide groups is almost complete, as evidenced by the disappearance of Si–OCH$_3$ signal. Since the hydrolytic

route produces a network with optimal condensation and cross-linking, the features of this specific formulation stem from the high amount of diphenyl-Si precursor, limiting the extent of condensation and full structural densification.

3.2. Optical measurements: excitation and fluorescence

The definition of the optical features of both as synthesized resins and doped, UV cured disks has been performed by excitation and fluorescence spectra (Fig. 8).

It is worth to observe the main features of the bare liquid resins in Fig. 8a and 8b. For the hydrolytic formulation DPDMM_M-H, with phenyl/Si molar ratio 0.40, the excitation maximum lies at 296 nm, while emission is at 350 nm. In the case of non-hydrolytic route, the resins DP50-NH and DPDM50-NH, with phenyl/Si molar ratio 1.00, show excitation maximum in both cases at 296 nm, while emission lies at 347 nm in the former and 338 nm in the latter. Previous literature extensively studied the optical properties of specific model compounds of phenyl containing polysiloxanes and polymers thereof in solution [41, 42], whereas few studies focused on solid state samples [43,44]. As for fluorescence emission, two main features are observed exciting phenylmethyl or dimethyl-co-diphenyl polysiloxanes, i.e. the monomer form and the excimer one. The monomer form is usually observed in diluted solution and is related to the -Si(C$_6$H$_5$)$_2$ isolated unit, whereas the excimer form arises from excitation of *triads* where diphenyl substituted trisiloxane units give rise to conformation with face-to-face phenyl rings, called *excimer forming sites*. In the present case, as evidenced by infrared analyses, we obtained macromolecules with alternated dimethyl-, diphenyl-, methacryloxypropyl-methoxy- units, as described in Figure S4 (SI).

Oligomers with vicinal units of diphenyl siloxane are not represented in Figure S4 but the high concentration of phenyl moieties supports the presence of these structures. Previous work with solid diphenyl-co-dimethyl polysiloxane evidenced similar features, since the emission is largely red-shifted at about 350 nm [43], with respect to similar formulations dissolved in THF where emission maximum is at 330 nm [45]. Therefore, in liquid state, the resins undiluted and highly viscous present strong intermolecular interactions, leading to stable excimers as in the solid state. Indeed, cross-linking sites exist even before UV curing, owing to the presence of trifunctional silane precursors, which *per se* favour the occurrence of tight, highly packed microstructures.

As for the photophysical properties of doped and UV cured solid samples, spectra of Fig. 8c and 8d, the excitation spectra recorded by
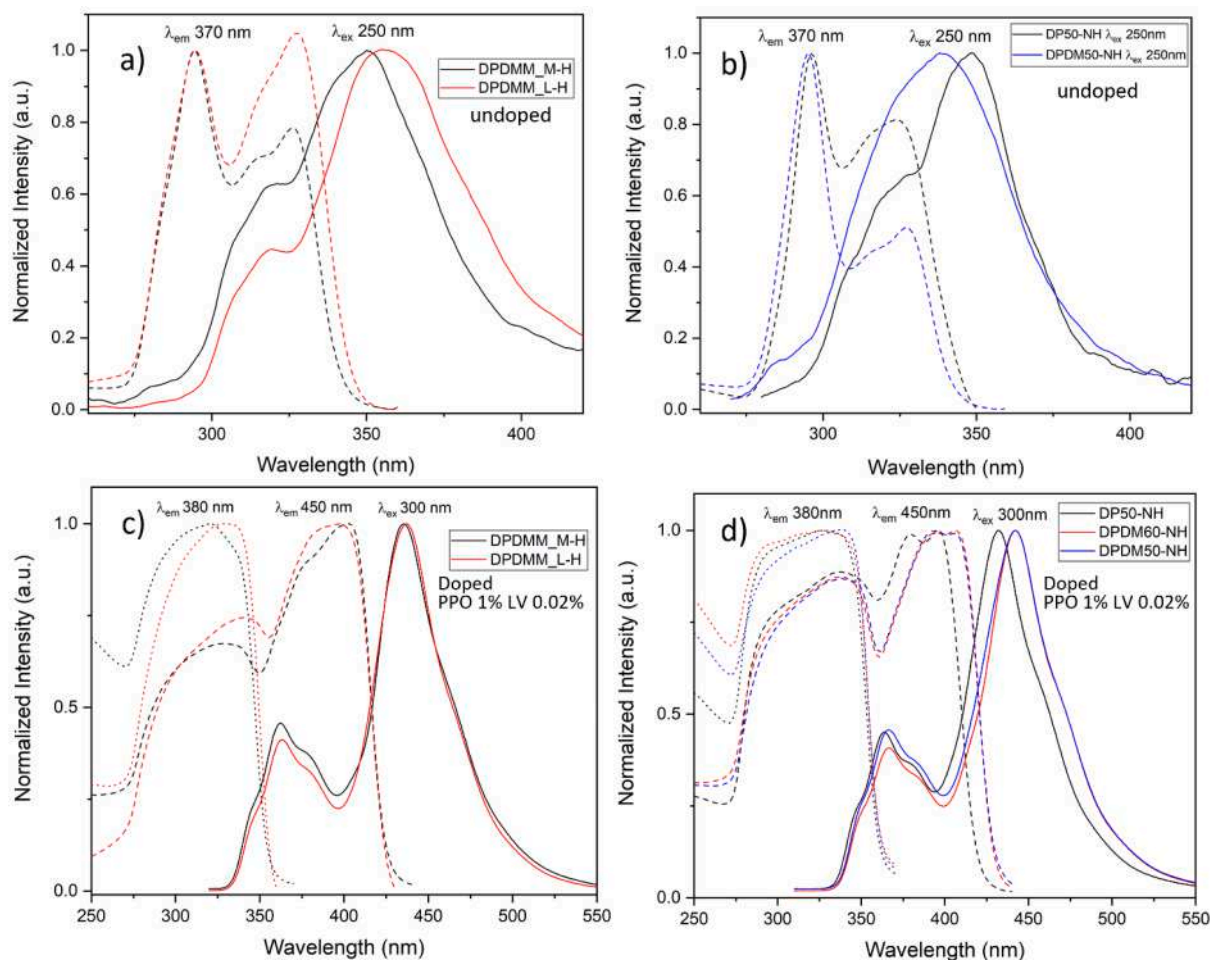
Fig. 8. Excitation and fluorescence spectra of the undoped as synthesized resins (a,b) and of UV cured doped resins (c,d) prepared by hydrolytic (a,c) and non-hydrolytic (b,d) pathways. For each spectrum, either excitation or emission, the selected wavelength to gather the excitation or emission spectrum is indicated on top. Excitation spectra are shown as dotted or dashed lines, while continuous line is used for emission. (For interpretation of the references to colour in this figure legend, the reader is referred to the web version of this article.)

collecting the signal at 380 nm show an intense signal spanning the range 280 - 340 nm, compatible with excitation of PPO, as previously shown for the case of PPO in siloxane matrix [46]. Collecting the emission at 450 nm, two components are visible, the most intense of which lies at 398–400 nm for DPDMM_L-H and DPDMM_M-H, at 396 nm for DP60-NH, while in the case of DPDM60-NH and DPDM50-NH it appears at 407 nm. This signal is ascribed to direct excitation of the wavelength shifter dye, Lumogen Violet, whose spectral features in dilute chloroform are characterized by an absorption maximum at 375 nm and emission at 410 nm, according to the literature [47]. The remarkable red shift in the excitation maximum might result from viscosity effects, besides stabilization of the dye molecule at the excited state due to the surrounding polysiloxane oligomers [48]. The chemical structure of Lumogen Violet, containing heteroatoms, carbonyl moieties and resonance structures may be largely affected by solvent polarizability and hydrogen bonding, hence a red shift in both excitation and fluorescence maxima is expected.

As for the lower intensity component, which appears in the range 290–350 nm, it can be ascribed to PPO as explained above, though a minor overlapping component could arise from the resin itself, as suggested by the spectral features of the undoped liquid polysiloxanes.

The fluorescence emission by exciting at 300 nm shows a two-component spectrum, with a low intensity band at 363 nm, corresponding to PPO emission, and a most intense one at about 440 nm, ascribed to Lumogen Violet. More in detail, the high intensity

component is at 432 nm for DP50-NH, at 436 nm for DPDMM_H—H and at 441 nm in the case of DPDM60-NH and DPDM50-NH samples. Considering the main outcome related to Si-OH unreacted groups, as evidenced by infrared spectroscopy, a correlation between maximum λ_{em} and the presence of these highly polar, hydrogen bonding moieties might be envisaged. LV belongs to the class of 1,8 naphthalimide derivatives [49] and photophysical properties of N-alkyl substituted 1,8-naphthalimides in solvent with varying polarity have been extensively studied. As an example, in the work of Marinova and co-workers [50]1,8-naphthalimide shows remarkable red-shift in emission maximum, with maximum at 421 nm in toluene and 443 nm in methanol. Therefore, as the dye is dissolved in environing media featuring highly polar nature and hydrogen bonding sites, the main emission undergoes remarkable red shift in agreement with our findings.

3.3. Scintillators light yield measurements

Analysis of light emitted under irradiation with α particles has been performed as described in the materials and methods section. Each pulse height spectrum, reported in Fig. 9a, represents a histogram of the total integral of the signals coming from the PMT output. Note that the total integral of each PMT signal is proportional to the energy released in the scintillator sample and to the light yield resulting from that specific event.

The waveforms, i.e. the decay time profile, are presented in Fig. 9b
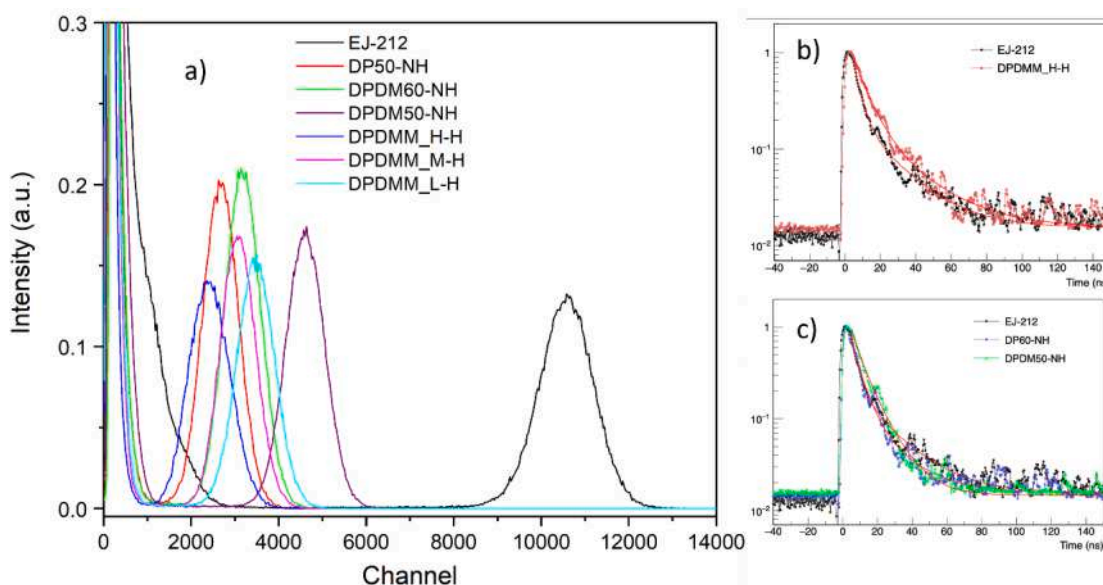
Fig. 9. a) Pulse height spectra of the UV cured siloxane disks under α irradiation and of the standard EJ-212 (a). Light pulse decay as average waveforms for selected samples, compared with the time profile of EJ-212 (b and c). (For interpretation of the references to colour in this figure legend, the reader is referred to the web version of this article.)

and 9c, for selected samples. The bi-exponential fitting function adopted to derive the kinetic parameters is:

$$I(t) = I_0 + (A_1/\tau_1)e^{-\frac{(t-t_0)}{\tau_1}} + (A_2/\tau_2)e^{-\frac{(t-t_0)}{\tau_2}} \qquad (1)$$

From eq. (1), the fast component (τ_1) and the slow one (τ_2) can be derived for each scintillator with relative abundance (A_1 and A_2), as reported in Table 2.

As for the light yield, it is worth to observe that the thickness of samples herein analysed as for light response varies in the range from 0.55 to 0.74 mm. Indeed, α particles do not deeply penetrate in the material, i. e. about 37 μm as proved by SRIM simulation [51] reported in Figure S5 (SI), thus the ionization events leading to generation of photons are confined to the superficial region. In our samples, the thickness variation from a sample to another is limited to 15%, therefore the difference in light path, though important, does not account for the collected difference in light yield. Rather, it is most likely that the presence of surface defects such as inhomogeneities or roughness can lead to appreciable variability in light yield. As a matter of fact, a tentative plot of light yield values versus phenyl molar content, which is known in literature to affect light yield [46], and sample thickness is reported in Figure S6, and no immediately conceivable relationship could be derived.

It is worth to note that all the samples are good scintillators, showing neat signals whose amplitude shows the same order of magnitude of the plastic standard, with a high value of 44% for the resin DPDM50-NH. As

for the response time of the scintillators, they show a double exponential decay, proper to organic based scintillators, with a fast component with decay in the order of ns and a slower one with decay of tens of ns. Usually, the time profile of the light pulse is acquired under irradiation with γ source, but in the present case the sample thickness is unsuited to gather a significant response under γ-rays, which are classified as low LET ionizing radiation. Therefore, the comparison between our data and literature ones is not straightforward, though in the case of EJ-212 the fast component of 3.73 ns is in good agreement with the manufacturer data (2.4 ns , Eljen Technology). In Table 2 the main features of the scintillators are reported, as for light yield and timing characteristics.

3.4. Photorheological tests

In-situ analysis of photoinduced cross-linking conducted on the prepared resins allows to select the most promising formulations and guides the choice of the proper parameters for the DLP printing process. Photorheology allows to derive the shear moduli as UV light is directed on a layer of the material, while minimal deformation is applied in a sinusoidal mode. Thus, the kinetics of photocuring is observed by the change in complex shear modulus, G*, defined as follows:
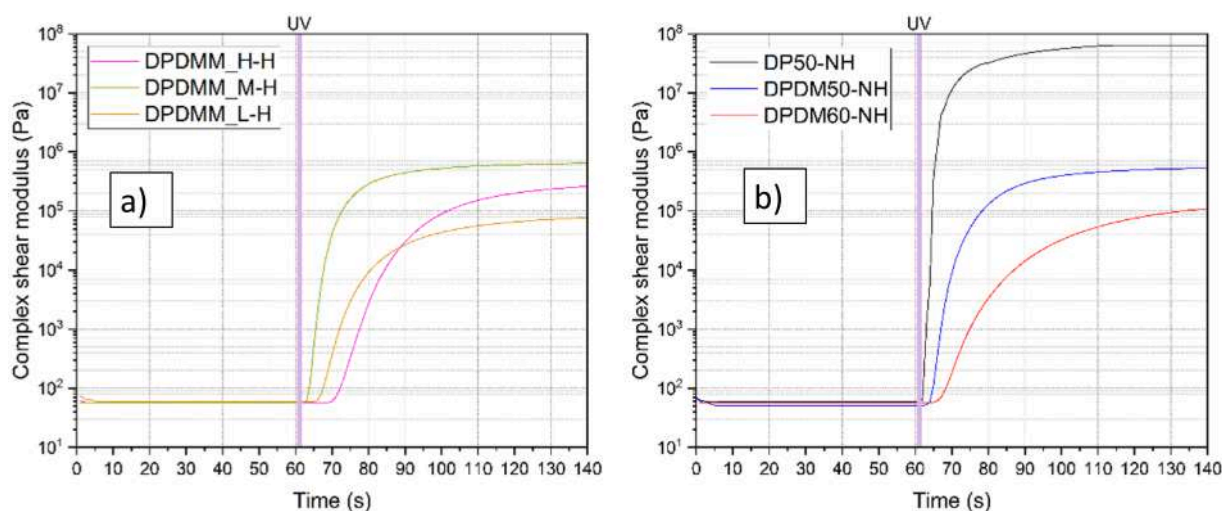
$$G^* = \sqrt{(G')^2 + (G'')^2} \qquad (2)$$

where G' and G'' stand for elastic and viscous modulus, respectively.

As the sample is irradiated, an increase of the complex shear modulus is observed, indicating that cross-linking takes place, leading to progressive decrease in chain mobility and consequent increase in stiffness of the network (see Fig. 10).

The increase of several orders of magnitude testifies the transition from liquid to solid, while the plateau reached after a definite time of irradiation indicates the completion of the photopolymerization and provides information on the stiffness of the cured material.

For DP50-NH the increase with time of G* is remarkably steep and starts immediately after UV light is turned on; moreover, the final value is the highest among the analysed formulations, reaching about 64 MPa. Conversely, the lowest G* is shown by the DPDMM_L-H resin, whose gentle slope under UV light ultimately leads to a value below 0.1 MPa; a slight delay in the onset of G* suggests that a higher critical energy dose is required to initiate photopolymerization.

Table 2
Scintillation properties of disk-shaped samples, thickness < 1 mm, doped with PPO 1% wt. and LV 0.02%wt. and irradiated with ^{241}Am α source. The values are expressed as% of light yield of a disk of EJ-212 0.5 mm thick. The decay time parameters (Eq. (1)) are also listed.

Sample	Thickness (mm)	Light Yield (%EJ)	τ_1 (ns) [σ]	A_1	τ_2 (ns) [σ]	A_2
DP50-NH	0.74	25 ± 4	4.7 ± 0.1	0.44	15.4 ± 0.4	0.56
DPDM50-NH	0.54	44 ± 5	6.5 ± 0.2	0.53	15.7 ± 0.7	0.47
DPDM60-NH	0.65	30 ± 4	6.4 ± 0.1	0.54	15.0 ± 0.6	0.46
DPDMM_H—H	0.57	23 ± 4	8.8 ± 0.2	0.54	52.6 ± 4.2	0.46
DPDMM_M-H	0.57	29 ± 4	5.6 ± 0.4	0.26	27.5 ± 2.8	0.74
DPDMM_L-H	0.57	33 ± 4	–	–	–	–
EJ-212	0.50	100	3.7 ± 0.1	0.40	19.5 ± 0.3	0.60

Fig. 10. Photorheology profiles of the UV curing process for the resins, either hydrolytic (a) or non-hydrolytic (b), added with TPO 1% wt. as initiator. The purple vertical line highlights the moment at which the UV light was switched on. (For interpretation of the references to colour in this figure legend, the reader is referred to the web version of this article.)

For the hydrolytic sol-gel process, the test allows to assess the catalyst contribution for a definite composition (Fig. 10a). The extensive literature on acid-catalyzed sol-gel process demonstrated that the pH of the starting sol plays a key role in the kinetics of hydrolysis and condensation, though our system is undoubtedly more complex than most studies on alkoxysilanes [52]. For low HCl concentration (0.1 M), incomplete condensation may be envisaged, and persistence of Si-OH as terminal or lateral ends of the oligomer is expected even after prolonged reaction time, as also evidenced by FTIR spectroscopy (Figure S1). The incomplete crosslinking produces oligomers with shorter chains, hence more limited steric interactions and entanglements between them; therefore, a prolonged exposure time and a higher extent of photopolymerization are required to increase the complex shear modulus G*. For high HCl concentration (1 M), on the other hand, the enhanced condensation of the gel produces long polymeric chains that inhibit diffusion and interaction of the photoreactive species. As a result, the onset of photopolymerization and the increase of G* are significantly delayed. Both compositions failed to reach a plateau in the observed time period; a medium HCl concentration (0.5 M) constitutes the best compromise between chain length and mobility, showing a rapid and steeper increase in G* and a plateau at ~0.6 MPa.

The non-hydrolytic resins are generally characterized by a steeper increase in G* as well as by a higher plateau value, due to the higher amount of acrylic, UV sensitive reactive substituents in the system (Table 1). Comparing the formulations DP50-NH, DPDM50-NH and DPDM60-NH, it is evident that addition of the dimethyl moiety leads to a decrease of the UV cured polysiloxane rigidity, as proved by the final G* value which drops to ~0.6 MPa and ~0.2 MPa for DPDM50-NH and DPDM60-NH, respectively. Moreover, in these formulations, the lower concentration of acrylic also accounts for a lower rate of photocrosslinking, as demonstrated by the gradual rise of G* with time after UV exposure. Unexpectedly, the delay is more evident for resin DPDM60-NH, despite the slightly higher amount of acrylic groups and lower amount of dimethyl groups. The reason could reside in the lower degree of condensation produced by the high amount of diphenyl groups, so that a higher degree of photocrosslinking is needed to generate a rigid network; also in this case, G* does not reach a plateau in the observed time window.

3.5. 3D printing of selected formulations through DLP

Specific criteria have driven the choice of the formulations to be printed by DLP:

- suitable kinetics for UV curing, i.e., rapid onset of curing and steep increase to a plateau value of complex shear modulus G*;
- moderately high final value of G*;
- high light yield.

For each printing test, the DLP printer has been configured with layer height and irradiation time per layer, besides being fed with the computer aided design shape, chosen as a model. All details are reported in Table 4.
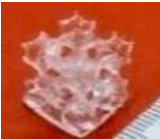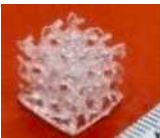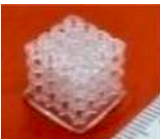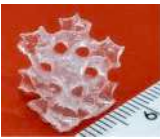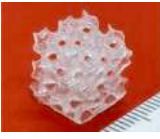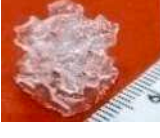
For each formulation the key parameters have been varied to optimize mechanical stability of the printed part under handling, quality of the print and minimal overexposure effect. This issue is due to excess of cure on the XY plane, leading to extension of the solidified portion beyond the imposed limits of the design and, at worst, to cavities closure. The preliminary curing experiments on ink droplets allow to define the promising parameters for DLP printing tests.

As expected, the curing depth reported in Table 3 follows the trends evidenced by the photorheological experiments, with the non-hydrolytic compositions displaying a generally higher curing depth peaked by DP50-NH at 1.38 mm. Among the hydrolytic compositions, DPDMM_M-H confirms to be a good candidate, with high curing depth and relatively good light yield. DPDMM_H—H and DPDMM_L-H show comparable curing depth (in Fig. 10a, they reach similar G* values after 30 s of exposure for an analogue thickness), although the latter shows a much higher light yield. Therefore, DPDMM_H—H has been excluded from the printing campaign. All other resins proved printable and optimal results have been achieved for each formulation, though in some cases fine adjustment in the parameters is required to get the best result, as detailed in Table 4. DP50NH shows the highest reactivity, allowing to print with short exposure times (3 s) and a high layer height (150 μm). DPDM50-NH proves similar printability, with only a slight increase in exposure times (4 s). The lower reactivity shown by DPDM60-NH

Table 3
Curing depth of the different resins irradiated at 30 mW/cm^2 for 30 s.

Resin	Curing depth (mm)
DP50-NH	1.38 ± 0.01
DPDM50-NH	1.25 ± 0.01
DPDM60-NH	0.60 ± 0.01
DPDMM_H—H	0.46 ± 0.01
DPDMM_M-H	0.97 ± 0.01
DPDMM_L-H	0.49 ± 0.01

Table 4

Resins used for DLP, set parameters, chosen shape as benchmark and final outcome. The UV light intensity was fixed at 30 mW/cm^2.

| Resin	Layer height (μm)	Irradiation time (s)	Shape	Comments	Photo
DP50-NH	150	3	Gyroid	Good, Rigid	
	150	3	Gyroid complex	Good, Rigid	
	150	3	Kelvin	Good, Rigid	
DPDM50-NH	150	4	Gyroid	Good	
	150	4	Gyroid complex	Good	
DPDM60-NH	50	8	Gyroid	Overexposed	
	75	10	Gyroid	Overexposed	
	100	10	Gyroid	Slightly overexposed	
DPDMM_M-H	50	12	Gyroid	Good	
DPDMM_L-H	50	16	Gyroid	Good	
	50	16	Gyroid	Good + 5 min in UV light furnace	
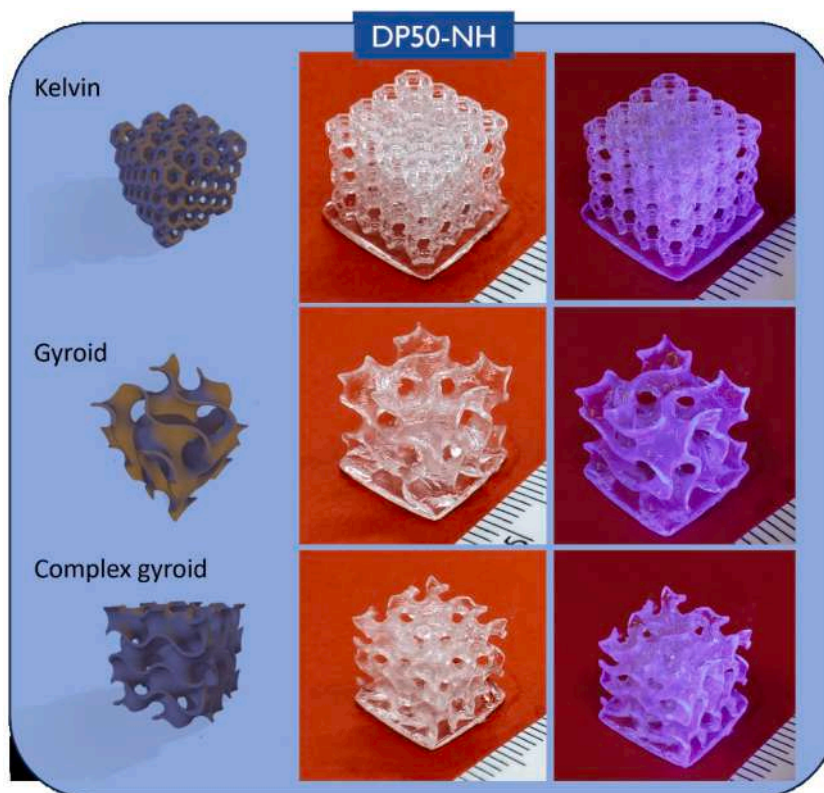
Fig. 11. Photos of the 3D printed objects obtained according to the CAD models on the left side. For resin DP50-NH, added with fluorophores, photos taken under ambient light (middle image) and UV light (right image) are shown.

requires an increase in exposure times up to 8–10 s, while the layer height is decreased to 50–100 μm. A reduced layer height provides for a higher resolution in Z direction; however, it also enhances the risk of overexposure, as evidenced in Table 4. While this phenomenon is generally counteracted by addition of photoabsorbers, here the transparency requirements prevent their use, hence a higher thickness has been selected. Printing experiments with the hydrolytic formulations are performed with a 50 μm layer height; no overexposure has been detected, probably due to the limited amount of acrylic in the systems. Even if it requires long exposure times (16 s), the less reactive DPMM_L-H still shows good printability; photocrosslinking may further progress through post-printing exposure under UV light for 5 min in a tabletop UV furnace, resulting in increased mechanical stability.

Examples of the different printed structures are reported in Fig. 11 for resin DP50-NH. Aiming at evidencing the printer capability to reproduce the CAD model, both the digital object and the corresponding printed component are shown. Photos taken under ambient light show that the material high transparency is retained through the printing process; its homogeneity is demonstrated by the uniform fluorescence displayed under UV light. Scanning Electron Microscopy evidences printing fidelity and resolution; exemplary images are reported for a Kelvin cell printed with resin DP50-NH and a gyroid printed with resin DPDMM_M-H (Fig. 12). The images show a good correspondence to the CAD files for both geometries and materials; the printed structures experienced a homogeneous linear shrinkage of ~20% compared to the model, caused by the crosslinking of the photopolymer and the evaporation of residual solvent. The feature size is also affected, and differences can be detected in the printing plane and along the print direction: in the DP50-NH Kelvin cell structure, the horizontal struts measure ~320 μm, in accordance with the overall linear shrinkage, whereas the vertical ones measure ~470 μm, demonstrating a slight overexposure of the printed layers. In the DPDMM_M-H gyroid structure, the walls

measure ~390 μm, indicating lower overexposure for this material. The effect of the layer height on the resolution is evident: in the DP50-NH Kelvin cell, the greater layer height (150 μm) results in a higher discretization of the inclined struts and in the appearance of the so-called "staircase effect"; on the gyroid printed with resin DPDMM_M-H and a layer height of 50 μm, the effect is still observed but does not affect the surface quality, allowing to better reproduce the smooth, curved surfaces of the CAD model.

Table 5 reports the results of the tensile test performed on DPDM50-NH and DPDM60-NH, since they represent the best compromise between printability and deformability of the cured materials (observed qualitatively). Moreover, the light yield values for these formulations are among the highest measured (44% the former, 30% the latter), then they were chosen for a full tensile characterization. In general, DPDM60-NH provided a better mechanical performance, with a tensile strength about 4 times higher than that of DPDM50-NH. The latter exhibits an elastic behaviour, whereas a deviation from linear elasticity, typical for elastomeric materials, is detected for DPDM60-NH samples. Printed specimens exhibited lower mechanical properties than cast ones for both compositions. This fact can be correlated with the presence of defects such as residual porosity, surface roughness and discontinuities between layers which are typical of the printing process. The infrared analyses show that for non-hydrolytic sol -gel derived samples containing dimethyl units unreacted silanols are present and, therefore, in both formulations final formation of oligomers can be envisaged, albeit photocuring appears to be carried out at an optimal extent at least in case of DPDM50-NH. As the higher amount of diphenyl silanes in DPDM60-NH inhibits the silanols condensation, the resulting network is composed of shorter oligomers able to deform to a higher extent and stand higher stresses. The elongation is significant for both compositions, but the highest values of strain at break (~40%) are in fact exhibited by DPDM60-NH cast samples; both materials are considered
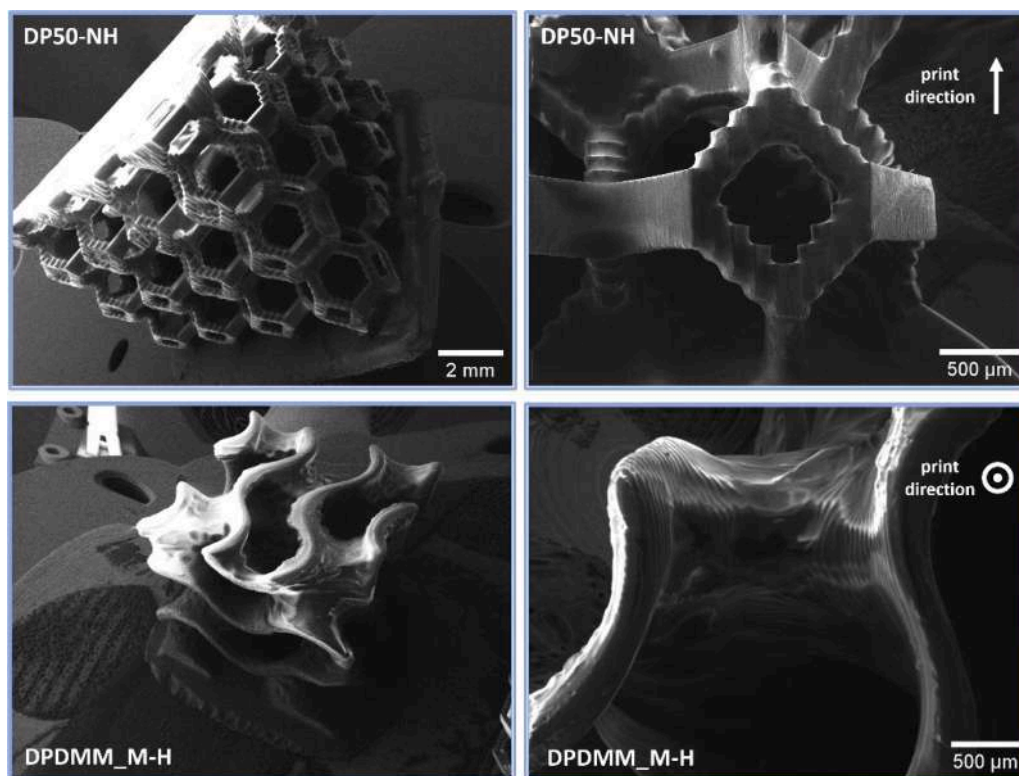
Fig. 12. Scanning Electron Microscope images of samples printed with DP50-NH (Kelvin cell, top panels) and DPDMM_M-H (Gyroid, bottom panels), taken at different magnifications to evidence the printing quality.

Table 5
Results of the tensile tests for DPDM50-NH and DPDM-60 NH: tensile fracture strength and strain at break, reported as mean value ± standard deviation.

Sample	Tensile fracture strength (MPa)	Strain at break (%)
DPDM50-NH cast	0.18 ± 0.05	21 ± 8
DPDM50-NH printed	0.07 ± 0.01	25 ± 2
DPDM60-NH cast	0.71 ± 0.17	40 ± 9
DPDM60-NH printed	0.39 ± 0.22	22 ± 8

compatible with the application, i.e. the production of flexible scintillators.

3.6. Proton beam irradiation of disks and 3D printed shapes

As a proof of concept to demonstrate the viability of using photo-crosslinked, DLP printed siloxane scintillators as proton detectors, the 3D printed shapes have been irradiated with 4.5 MeV H^+ at the CN accelerator (LNL-INFN). Selected disks and DLP printed samples have been placed on a movable sample holder. As protons impinge on the sample positioned along the beam line, the scintillation light emitted is gathered by the CCD camera and images are recorded either every 0.05 s or 1 s. In Fig. 13 the experimental set-up is described and the results of beam irradiation on disks and 3D printed samples are reported.

As mentioned previously, the beam current is not stable during the measurements run, varying in the range 16 – 18 nA. However, the results are extremely encouraging as for response and signal endurance upon irradiation with protons. Notwithstanding the clearly higher luminosity of EJ-212, all the samples either 3D printed or cast moulded show an intense and stable signal, with the beam spot contours neatly distinguishable and with the luminosity trend as expected from the light yield results. In Fig. 13c the samples have been irradiated for 102 s, thus a fluence of 3×10^{13} H^+/cm^2 has been reached with no obvious variation in signal intensity, thus hinting a good radiation resistance.

4. Conclusions

Flexible 3D-printed siloxane-based scintillators have been successfully produced and tested under ion beam irradiation. Two different sol-gel routes have been applied to synthesize phenyl-bearing siloxane resins with methacrylate functionalities photopolymerizable by UV illumination and suitable to be shaped at desired 3D geometries through DLP. FTIR spectroscopy shows that both approaches, hydrolytic and non-hydrolytic, led to the successful formation of the siloxane-based network as highlighted by the intense band of the Si-O-Si bridging bonds and to an optimal extent of the photocuring process as indicated by the disappearance of the vinyl peak.

Optical clarity of all the UV photocured samples is particularly high except in the case of hydrolytic synthesis at high HCl concentration, where a slight yellowing was observed. Fluorescence and excitation optical measurements demonstrate the ability of the produced siloxanes to dissolve the fluorophores necessary to generate photoluminescence while maintaining their optical properties even after photocuring.

Scintillation measurements under α irradiation highlight that all the produced polysiloxanes are good scintillators with signal amplitudes in the same order of magnitude of the standard plastic scintillator, reaching a value as remarkable as 44% for the DPDM50-NH formulation.

Photorheological tests allowed to point out the different kinetics of photoinduced curing in the produced samples, characterized by different photopolymerization onset, curing time and final stiffness depending on the synthesis parameters used.

Specific formulations obtained by either process have been selected based on the rheological properties and light yield and printed by DLP in the form of benchmark shapes such as gyroid and Kelvin cell. All the resins proved printable and optimal results have been obtained, with exposure times ranging from 3 to 16 s and layer height from 50 to 150 μm. The high optical transparency was retained through the printing process and a homogeneous linear shrinkage around 20% was observed. Good printing resolution has been revealed by SEM images, increasing
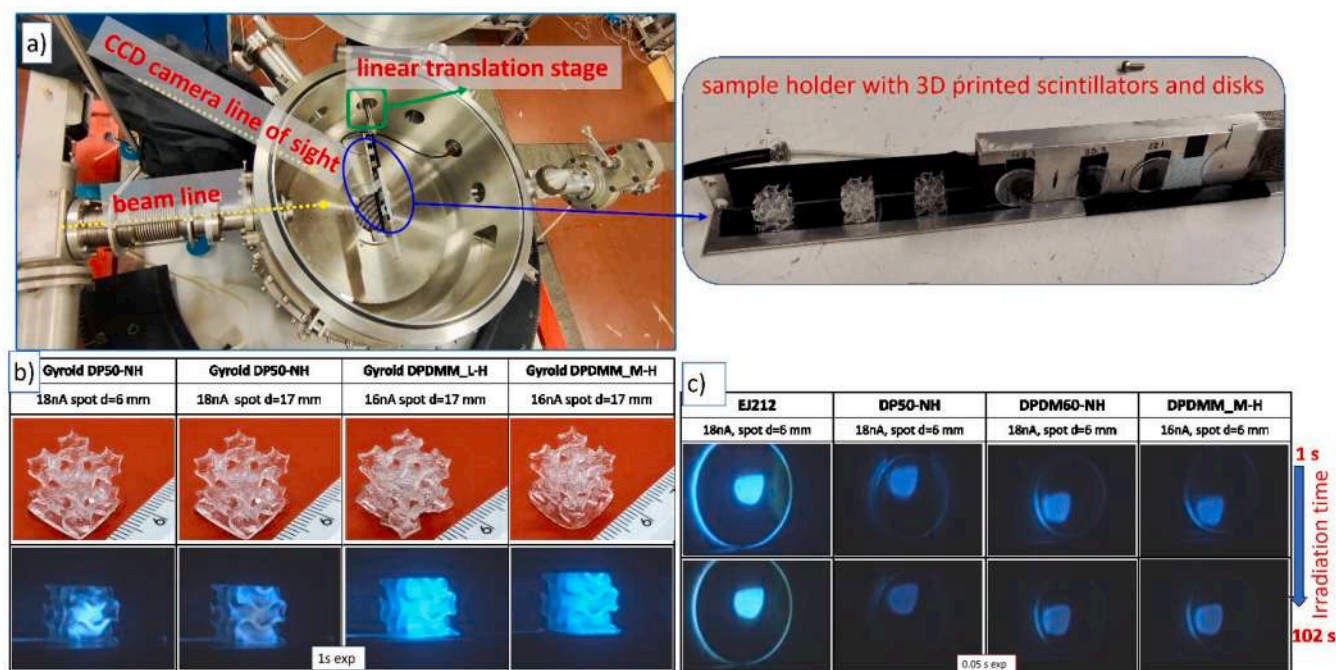
Fig. 13. (a) Photo of the experimental set-up used for 4.5 MeV H^+ irradiation with zoomed view of the sample holder and (b) images of the DLP printed shapes (exposure time 1 s; for the sample DP50-NH the image obtained with small spot size beam is also reported) and (c) the thin disks obtained by casting collected with the CCD camera under irradiation (exposure time 0.05 s). In (c) the images after 1 s of irradiation and after 102 s are reported (exposure time 0.05 s).

as the layer height decreases.

As for scintillation, beyond the test with calibration α source, the cured samples and 3D printed complex shapes showed bright light signal under irradiation with proton beam at 4.5 MeV gathered with ease by the CCD camera, coupled to the view port of the scattering chamber of the beam line. Neat images of the beam spot have been recorded with no sign of deterioration in luminosity even after high total fluence on the 3D printed scintillators. Therefore, the set of experimental results herein reported stand as unambiguous proof of concept that a new class of 3D printed silicone-based scintillators is currently in the limelight, with the practical benefits that this may entail in nuclear, high energy and medical physics applications.

CRediT authorship contribution statement

Sara Maria Carturan: Writing – review & editing, Writing – original draft, Visualization, Validation, Supervision, Software, Resources, Project administration, Methodology, Investigation, Funding acquisition, Formal analysis, Data curation, Conceptualization. **Hanna Skliarova:** Writing – review & editing, Validation, Methodology, Investigation, Data curation, Conceptualization. **Giorgia Franchin:** Writing – review & editing, Writing – original draft, Visualization, Validation, Supervision, Software, Methodology, Investigation, Funding acquisition, Formal analysis, Data curation, Conceptualization. **Giada Bombardelli:** Methodology, Investigation, Data curation. **Alice Zanini:** Writing – review & editing, Validation, Methodology, Investigation, Data curation. **Felix Eduardo Pino Andrades:** Writing – original draft, Methodology, Investigation, Formal analysis, Data curation, Conceptualization. **Jessica Carolina Delgado Alvarez:** Methodology, Formal analysis, Data curation. **Sandra Moretto:** Writing – review & editing, Methodology, Investigation, Formal analysis, Data curation, Conceptualization. **Gianluigi Maggioni:** Writing – review & editing, Methodology, Investigation, Conceptualization. **Walter Raniero:** Writing – review & editing, Software, Methodology. **Devid Maniglio:** Writing – review & editing, Project administration, Methodology, Investigation. **Anna Paola Caricato:** Writing – review & editing, Resources, Project administration, Funding acquisition. **Alberto Quaranta:** Writing – review & editing, Supervision, Resources, Methodology, Funding acquisition, Data curation, Conceptualization.

Declaration of competing interest

The authors declare that they have no known competing financial interests or personal relationships that could have appeared to influence the work reported in this paper.

Data availability

Data will be made available on request.

Acknowledgments

Supplementary materials

Supplementary material associated with this article can be found, in the online version, at doi:10.1016/j.apmt.2024.102313.

References

[1] M. Pari, G. Ballerini, A. Berra, R. Boanta, M. Bonesini, C. Brizzolari, G. Brunetti, M. Calviani, S. Carturan, M.G. Catanesi, S. Cecchini, A. Coffani, F. Cindolo, G. Collazuol, E. Conti, F. Dal Corso, G. De Rosa, C. Delogu, A. Gola, R.A. Intonti, C. Jollet, Y. Kudenko, M. Laveder, A. Longhin, P.F. Loverre, L. Ludovici, L. Magaletti, G. Mandrioli, A. Margotti, V. Mascagna, N. Mauri, A. Meregaglia, M. Mezzetto, M. Nessi, A. Paoloni, E. Parozzi, L. Pasqualini, G. Paternoster, L. Patrizii, C. Piemonte, M. Pozzato, F. Pupilli, M. Prest, E. Radicioni, C. Riccio, A. C. Ruggeri, G. Sirri, M. Soldani, M. Tenti, M. Torti, F. Terranova, E. Vallazza, M. Vesco, L. Votano, Shashlik calorimeters: Novel compact prototypes for the ENUBET experiment, Nucl Instrum Methods Phys Res A (2019) 936, https://doi.org/10.1016/j.nima.2018.11.041.
[2] A. Boyarintsev, A. De Roeck, S. Dolan, A. Gendotti, B. Grynyov, U. Kose, S. Kovalchuk, T. Nepokupnaya, A. Rubbia, D. Sgalaberna, T. Sibilieva, X.Y. Zhao, Demonstrating a single-block 3D-segmented plastic-scintillator detector, Journal of Instrumentation 16 (2021) P12010, https://doi.org/10.1088/1748-0221/16/12/P12010.
[3] A. Blondel, F. Cadoux, S. Fedotov, M. Khabibullin, A. Khotjantsev, A. Korzenev, A. Kostin, Y. Kudenko, A. Longhin, A. Mefodiev, P. Mermod, O. Mineev, E. Noah, D. Sgalaberna, A. Smirnov, N. Yershov, A fully-active fine-grained detector with three readout views, Journal of Instrumentation 13 (2018), https://doi.org/10.1088/1748-0221/13/02/P02006. P02006–P02006.
[4] L. Beaulieu, S. Beddar, Review of plastic and liquid scintillation dosimetry for photon, electron, and proton therapy, Phys Med Biol 61 (2016) R305–R343, https://doi.org/10.1088/0031-9155/61/20/R305.
[5] M. Almurayshid, Y. Helo, A. Kacperek, J. Griffiths, J. Hebden, A. Gibson, Quality assurance in proton beam therapy using a plastic scintillator and a commercially available digital camera, J Appl Clin Med Phys 18 (2017) 210–219, https://doi.org/10.1002/acm2.12143.
[6] F. Alsanea, C. Darne, D. Robertson, S. Beddar, Ionization quenching correction for a 3D scintillator detector exposed to scanning proton beams, Phys Med Biol 65 (2020) 075005, https://doi.org/10.1088/1361-6560/ab7876.
[7] S.M. Goddu, G.T. Westphal, B. Sun, Y. Wu, C.D. Bloch, J.D. Bradley, A. Darafsheh, Synchronized high-speed scintillation imaging of proton beams, generated by a gantry-mounted synchrocyclotron, on a pulse-by-pulse basis, Med Phys 49 (2022) 6209–6220, https://doi.org/10.1002/mp.15826.
[8] S. Beddar, 3D dosimetry for proton therapy, J Phys Conf Ser 1305 (2019) 6–11, https://doi.org/10.1088/1742-6596/1305/1/012038.
[9] L. Archambault, J.C. Polf, L. Beaulieu, S. Beddar, Characterizing the response of miniature scintillation detectors when irradiated with proton beams, Phys Med Biol 53 (2008) 1865–1876, https://doi.org/10.1088/0031-9155/53/7/004.
[10] S. Calvi, L. Basiricò, S.M. Carturan, I. Fratelli, A. Valletta, A. Aloisio, S. De Rosa, F. Pino, M. Campajola, A. Ciavatti, L. Tortora, M. Rapisarda, S. Moretto, M. Verdi, S. Bertoldo, O. Cesarini, P. Di Meo, M. Chiari, F. Tommasino, E. Sarnelli, L. Mariucci, P. Branchini, A. Quaranta, B. Fraboni, Flexible fully organic indirect detector for megaelectronvolts proton beams, Npj Flexible Electronics 7 (2023) 1–11, https://doi.org/10.1038/s41528-022-00229-w.
[11] S. Berns, E. Boillat, A. Boyarintsev, A. De Roeck, S. Dolan, A. Gendotti, B. Grynyov, S. Hugon, U. Kose, S. Kovalchuk, B. Li, A. Rubbia, T. Sibilieva, D. Sgalaberna, T. Weber, J. Wuthrich, X.Y. Zhao, Additive manufacturing of fine-granularity optically-isolated plastic scintillator elements, Journal of Instrumentation 17 (2022), https://doi.org/10.1088/1748-0221/17/10/P10045.
[12] N. Lynch, T. Monajemi, J.L. Robar, Characterization of novel 3D printed plastic scintillation dosimeters, Biomed Phys Eng Express 6 (2020), https://doi.org/10.1088/2057-1976/aba880.
[13] D.G. Kim, K. Kim, S. Lee, Y.K. Kim, Enhanced characteristics of 3D-Printed plastic scintillators based on bisphenol fluorene diacrylates, Radiation Physics and Chemistry 198 (2022) 110255, https://doi.org/10.1016/j.radphyschem.2022.110255.
[14] J. Son, D.G. Kim, S. Lee, J. Park, Y. Kim, T. Schaarschmidt, Y.K. Kim, Improved 3D Printing Plastic Scintillator Fabrication, Journal of the Korean Physical Society 73 (2018) 887–892, https://doi.org/10.3938/jkps.73.887.
[15] F.D. Brooks, Development of organic scintillators, Nuclear Instruments and Methods 162 (1979) 477–505, https://doi.org/10.1016/0029-554X(79)90729-8.
[16] C. Chandler, D.H. Porcincula, M.J. Ford, T.J. Kolibaba, B. Fein-Ashley, J. Brodsky, J.P. Killgore, A. Sellinger, Influence of fluorescent dopants on the vat photopolymerization of acrylate-based plastic scintillators for application in neutron/gamma pulse shape discrimination, Addit Manuf 73 (2023), https://doi.org/10.1016/j.addma.2023.103688.
[17] T.H. Kim, S. Lee, D.G. Kim, J.Y. Jeong, H.J. Yang, T. Schaarschmidt, S.H. Choi, G. S. Cho, Y.K. Kim, H.T. Chung, A feasibility study of using a 3D-printed tumor model scintillator to verify the energy absorbed to a tumor, Nuclear Engineering and Technology 53 (2021) 3018–3025, https://doi.org/10.1016/j.net.2021.03.033.
[18] D.Kulig Kapłon, S. Beddar, T. Fiutowski, W. Górska, J. Hajduga, P. Jurgielewicz, D. Kabat, K. Kalecińska, M. Kopeć, S. Koperny, B. Mindur, J. Moroń, G. Moskal, S. Niedźwiecki, M. Silarski, F. Sobczuk, T. Szumlak, A. Ruciński, Investigation of the light output of 3D-printed plastic scintillators for dosimetry applications, Radiat Meas 158 (2022), https://doi.org/10.1016/j.radmeas.2022.106864.
[19] S.M. Carturan, A. Quaranta, Polysiloxane-Based Scintillators, in: M. Hamel (Ed.), Plastic scintillators, Springer Cham, 2021, pp. 169–199, https://doi.org/10.1007/978-3-030-73488-6.
[20] J. Arrue, C. Chandler, M. Duce, A. Lim, A. Sellinger, A. Erickson, Impact of temperature on light yield and pulse shape discrimination of polysiloxane-based organic scintillators formulated with commercial resins, Nucl Instrum Methods Phys Res A (2023) 1056, https://doi.org/10.1016/j.nima.2023.168650.
[21] A. Lim, J. Arrue, P.B. Rose, A. Sellinger, A.S. Erickson, Polysiloxane Scintillators for Efficient Neutron and Gamma-Ray Pulse Shape Discrimination, ACS Appl Polym Mater 2 (2020) 3657–3662, https://doi.org/10.1021/acsapm.0c00641.
[22] G Aldosary, J Belec, C Foottit, E. Vandervoort, Dosimetric considerations for moldable silicone composites used in radiotherapy applications, J Appl Clin Med Phys 23 (2022) e13605, https://doi.org/10.1002/acm2.13605.
[23] A. Duetschler, L. Huang, G. Fattori, G. Meier, C. Bula, J. Hrbacek, S. Safai, D. C. Weber, A.J. Lomax, Y. Zhang, A motion model-guided 4D dose reconstruction for pencil beam scanned proton therapy, Phys Med Biol 68 (11) (2023), https://doi.org/10.1088/1361-6560/acd518, 68May 30.
[24] M. Mohseni, S. Bastani, A. Jannesari, Effects of silane precursors on curing behavior of UV-curable hybrid coatings: A photo-DSC study, J Therm Anal Calorim 119 (2015) 515–526, https://doi.org/10.1007/s10973-014-4071-1.
[25] H.E. Lee, D. Lee, T.I. Lee, J. Jang, J. Jang, Y.W. Lim, J.H. Shin, S.M. Kang, G. M. Choi, D.J. Joe, J.H. Kim, S.H. Lee, S.H. Park, C.B. Park, T.S. Kim, K.J. Lee, B. S. Bae, Siloxane Hybrid Material-Encapsulated Highly Robust Flexible μLEDs for Biocompatible Lighting Applications, ACS Appl Mater Interfaces 14 (2022) 28258–28269, https://doi.org/10.1021/acsami.2c03922.
[26] X. Yang, Q. Chen, H. Bao, J. Liu, Y. Wu, G. Lai, Preparation and performance of ultraviolet curable silicone resins used for ultraviolet cured coating and ultraviolet-assisted 3D printing materials, OSA Contin 1 (2018) 542, https://doi.org/10.1364/osac.1.000542.
[27] S. Jana, M.A. Lim, I.C. Baek, C.H. Kim, S. Il Seok, Non-hydrolytic sol-gel synthesis of epoxysilane-based inorganic-organic hybrid resins, Mater Chem Phys 112 (2008) 1008–1014, https://doi.org/10.1016/j.matchemphys.2008.06.070.
[28] D.G. Kim, K. Kim, S. Lee, Y.K. Kim, Enhanced Characteristics of 3D-Printed Plastic Scintillators Based on Bisphenol Fluorene Diacrylates, Rad Phys 198 (2022) 110255, https://doi.org/10.1016/j.radphyschem.2022.110255.
[29] J. Jin, S. Yang, B.S. Bae, Fabrication of a high thermal-stable methacrylate-silicate hybrid nanocomposite: Hydrolytic versus non-hydrolytic sol-gel synthesis of methacryl-oligosiloxanes, J Solgel Sci Technol 61 (2012) 321–327, https://doi.org/10.1007/s10971-011-2630-5.
[30] R. Buestrich, F. Kahlenberg, M. Popall, P. Dannberg, et al., ORMOCER®s for Optical Interconnection Technology, Journal of Sol-Gel Science and Technology 20 (2001) 181–186, https://doi.org/10.1023/A:1008755607488.
[31] J.S. Kim, S. Yang, B.S. Bae, Thermally stable transparent sol-gel based siloxane hybrid material with high refractive index for light emitting diode (LED) encapsulation, Chemistry of Materials 22 (2010) 3549–3555, https://doi.org/10.1021/cm100903b.
[32] C.L. Fontana, M. Lunardon, F.E. Pino, L. Stevanato, A. Carnera, C. Sada, F. Soramel, S. Moretto, A distributed data acquisition system for signal digitizers with on-line analysis capabilities, in: 2017 IEEE Nuclear Science Symposium and Medical Imaging Conference, NSS/MIC 2017 - Conference Proceedings, 2018, https://doi.org/10.1109/NSSMIC.2017.8533063.
[33] M. Pantoja, B. Díaz-Benito, F. Velasco, J. Abenojar, J.C. del Real, Analysis of hydrolysis process of γ-methacryloxypropyltrimethoxysilane and its influence on the formation of silane coatings on 6063 aluminum alloy, Appl Surf Sci 255 (2009) 6386–6390, https://doi.org/10.1016/j.apsusc.2009.02.022.
[34] S. Cui, Y. Liu, M.H. Fan, A.T. Cooper, B.L. Lin, X.Y. Liu, G.F. Han, X.D. Shen, Temperature dependent microstructure of MTES modified hydrophobic silica aerogels, Mater Lett 65 (2011) 606–609, https://doi.org/10.1016/j.matlet.2010.11.026.
[35] Y.S. Li, Y. Wang, S. Ceesay, Vibrational spectra of phenyltriethoxysilane, phenyltrimethoxysilane and their sol-gels, Spectrochim Acta A Mol Biomol Spectrosc 71 (2009) 1819–1824, https://doi.org/10.1016/j.saa.2008.04.027.
[36] J.S. Kim, S.C. Yang, S.Y. Kwak, Y. Choi, K.W. Paik, B.S. Bae, High performance encapsulant for light-emitting diodes (LEDs) by a sol-gel derived hydrogen siloxane hybrid, J Mater Chem 22 (2012) 7954–7960, https://doi.org/10.1039/c2jm16907j.
[37] P. Rodič, J. Iskra, I. Milošev, A hybrid organic-inorganic sol-gel coating for protecting aluminium alloy 7075-T6 against corrosion in Harrison's solution, J Solgel Sci Technol 70 (2014) 90–103, https://doi.org/10.1007/s10971-014-3278-8.
[38] R. Buestrich, F. Kahlenberg, M. Popall, P. Dannberg, R. Müller- Fiedler, O. Rösch, ORMOCER ® s for Optical Interconnection Technology, J Solgel Sci Technol 20 (2001) 181–186, https://doi.org/10.1023/A:1008755607488.
[39] Y.J. Eo, T.H. Lee, S.Y. Kim, J.K. Kang, Y.S. Han, B.S. Bae, Synthesis and molecular structure analysis of nano-sized methacryl-grafted polysiloxane resin for fabrication of nano hybrid materials, J Polym Sci B Polym Phys 43 (2005) 827–836, https://doi.org/10.1002/polb.20346.
[40] J.S. Kim, S.C. Yang, B.S. Bae, Thermal stability of sol-gel derived methacrylate oligosiloxane-based hybrids for LED encapsulants, J Solgel Sci Technol 53 (2010) 434–440, https://doi.org/10.1007/s10971-009-2117-9.
[41] T. Itoh, Spectroscopy and photophysics of methylphenylsiloxaneand diphenylsiloxane-based molecules and polymers, Research on Chemical Intermediates 27 (2001) 669–685, https://doi.org/10.1163/156856701317051761.

[42] C. Salom, A. Horta, I. Hernandez-fuentes, I.F. Pierola, Poly(phenylsiloxanes) Electronic Spectra, Macromolecules 20 (1987) 696–698, https://doi.org/10.1021/ma00169a041.

[43] L. Zhu, X. Cheng, W. Su, J. Zhao, C. Zhou, Molecular insights into sequence distributions and conformation-dependent properties of high-phenyl polysiloxanes, Polymers (Basel) (2019) 11, https://doi.org/10.3390/polym11121989.

[44] A. Quaranta, S. Carturan, M. Cinausero, T. Marchi, F. Gramegna, M. Degerlier, A. Cemmi, S. Baccaro, Characterization of polysiloxane organic scintillators produced with different phenyl containing blends, Mater Chem Phys 137 (2013), https://doi.org/10.1016/j.matchemphys.2012.10.041.

[45] T. Itoh, M.H. Yang, Temperature dependence of the fluorescence quantum yields of diphenylsiloxane-based copolymers in dilute solutions, J Polym Sci B Polym Phys 40 (2002) 854–861, https://doi.org/10.1002/polb.10151.

[46] A. Quaranta, S.M. Carturan, T. Marchi, V.L. Kravchuk, F. Gramegna, G. Maggioni, M. Degerlier, Optical and scintillation properties of polydimethyl-diphenylsiloxane based organic scintillators, IEEE Trans Nucl Sci 57 (2010) 891–900, https://doi.org/10.1109/TNS.2010.2042817.

[47] M.D. Palma, A. Quaranta, T. Marchi, G. Collazuol, S. Carturan, M. Cinausero, M. Degerlier, F. Gramegna, Red emitting phenyl-polysiloxane based scintillators for neutron detection, IEEE Trans Nucl Sci 61 (2014) 2052–2058, https://doi.org/10.1109/TNS.2014.2302036.

[48] B. Valeur, Molecular Fluorescence, Wiley, 2001, https://doi.org/10.1002/3527600248.

[49] K. Jo, S. Lee, A. Yi, T.-Y. Jeon, H.H. Lee, D. Moon, D.M. Lee, J. Bae, S.-T. Hong, J. Gene, ‖ Seung, G. Lee, H.J. Kim, Alkyl Conformation and π−π Interaction Dependent on Polymorphism in the 1,8-Naphthalimide (NI) Derivative, ACS Omega 4 (2019) 19705–19709, https://doi.org/10.1021/acsomega.9b02377.

[50] N.V. Marinova, N.I. Georgiev, V.B. Bojinov, Facile synthesis, sensor activity and logic behaviour of 4-aryloxy substituted 1,8-naphthalimide, J Photochem Photobiol A Chem 254 (2013) 54–61, https://doi.org/10.1016/j.jphotochem.2013.01.008.

[51] J.F. Ziegler, M.D. Ziegler, J.P. Biersack, SRIM – The stopping and range of ions in matter (2010), Nucl Instrum Methods Phys Res B 268 (2010) 1818–1823, https://doi.org/10.1016/j.nimb.2010.02.091.

[52] C.J. Brinker, G.W. Scherer, Sol-Gel Science: The Physics and Chemistry of Sol-Gel Processing, Sol-Gel Science: The Physics and Chemistry of Sol-Gel Processing (2013) 1–908, https://doi.org/10.1016/C2009-0-22386-5.